Effect of Microcomputed Tomography Voxel Size on the Finite Element Model Accuracy for Human Cancellous Bone

Yener N. Yeni
e-mail: yeni@bjc.hfh.edu

Gregory T. Christopherson

X. Neil Dong

Do-Gyoon Kim

David P. Fyhrie

Bone and Joint Center, Henry Ford Hospital, Detroit, MI

The level of structural detail that can be acquired and incorporated in a finite element (FE) analysis might greatly influence the results of microcomputed tomography (μCT)-based FE simulations, especially when relatively large bones, such as whole vertebrae, are of concern. We evaluated the effect of scanning and reconstruction voxel size on the μCT-based FE analyses of human cancellous tissue samples for fixed- and free-end boundary conditions using different combinations of scan/reconstruction voxel size. We found that the bone volume fraction (BV/TV) did not differ considerably between images scanned at 21 and 50 μm and reconstructed at 21, 50, or 110 μm (-0.5% to 7.8% change from the 21/21 μm case). For the images scanned and reconstructed at 110 μm, however, there was a large increase in BV/TV compared to the 21/21 μm case (58.7%). Fixed-end boundary conditions resulted in 1.8% [coefficient of variation (COV)] to 14.6% (E) difference from the free-end case. Dependence of model output parameters on scanning and reconstruction voxel size was similar between free- and fixed-end simulations. Up to 26%, 30%, 17.8%, and 32.3% difference in modulus (E), and average (VMExp), standard deviation (VMSD) and coefficient of variation (COV) of von Mises stresses, respectively, was observed between the 21/21 μm case and other scan/reconstruction combinations within the same (free or fixed) simulation group. Observed differences were largely attributable to scanning resolution, although reconstruction resolution also contributed significantly at the largest voxel sizes. All 21/21 μm results (taken as the gold standard) could be predicted from the 21/50 ($r^2_{adj}=0.91-0.99; p<0.001$), 21/110 ($r^2_{adj}=0.58-0.99; p<0.02$) and 50/50 results ($r^2_{adj}=0.61-0.97; p<0.02$). While BV/TV, VMSD, and $VMExp/\sigma_z$ from the 21/21 could be predicted by those from the 50/110 ($r^2_{adj}=0.63-0.93; p<0.02$) and 110/110 ($r^2_{adj}=0.41-0.77; p<0.05$) simulations as well, prediction of E, VMExp, and COV became marginally significant ($0.04<p<0.13$) at 50/110 and nonsignificant at 110/110 ($0.21<p<0.70$). In conclusion, calculation of cancellous bone modulus, mean trabecular stress, and other parameters are subject to large errors at 110/110 μm voxel size. However, enough microstructural details for studying bone volume fraction, trabecular shear stress scatter, and trabecular shear stress amplification ($VMExp/\sigma_z$) can be resolved using a 21/110 μm, 50/110 μm, and 110/110 μm voxels for both free- and fixed-end constraints. [DOI: 10.1115/1.1835346]

Keywords: Microcomputed Tomography, Finite Element Method, Voxel Size, Element Size, Boundary Conditions, Accuracy, Trabecular Bone

Introduction

It is estimated that 4–6 million women and 1–2 million men currently have osteoporosis in the United States and a dramatic increase in numbers is expected in the next few decades [1]. Although much of the mortality and morbidity due to osteoporosis-related fractures are associated with those of the hip [2,3], pain and disability associated with fracture of the spine is no less of a problem, especially when the fact that 50% of the elderly female population is expected to have at least one vertebral fracture is considered [4–6]. Overall, the direct medical cost of fractures associated with osteoporosis is 10.3 to 15.2 billion dollars in the US alone [1].

Mechanically, fracture risk of a structure is determined by the mechanical properties of the structure and the external loads to which the structure is subjected. For all external loads being equal, bones with greater strength have less chance for fracture. The current World Health Organization definition of osteoporosis [bone mineral density (BMD), 2.5 standard deviations below the mean of young normal white women [7]] inherently assumes BMD as a surrogate for bone strength. A more mechanistic prediction of bone strength would not only provide a means for consistent diagnostic tools but also a basis for the development of prevention and treatment modalities through a better understanding of the underlying mechanisms by which bone forms its mechanical properties.

Vertebrae mostly consist of cancellous bone that provide the vertebra with the great majority of its mechanical properties [8]. The thin cortical shell surrounding the vertebra also makes a substantial contribution to the mechanical competence of the whole vertebra [9–12], especially when the cancellous bone is weakened due to osteoporosis [10]. Therefore, the capacity to analyze an entire vertebral body is important for a better understanding of whole bone behavior.

Computed tomography (CT)-based finite element (FE) analysis has proven useful for examining the mechanical behavior of

Contributed by the Bioengineering Division for publication in the JOURNAL OF BIOMECHANICAL ENGINEERING. Manuscript received by the Bioengineering Division December 22, 2004; revised manuscript received August 18, 2004. Associate Editor: Jeffrey A. Weiss.

whole bones as well as for examining microstructural aspects of cancellous bone tissue. The use of CT for these analyses is becoming increasingly popular because of the nondestructive nature of the application. However, the level of structural detail that can be acquired by tomography scans and incorporated in the FE analysis might greatly influence the results from cancellous bone tissue [13–15] and also from relatively large bones [16]. Crawford et al. [17] recently investigated the effect of element size on the FE-calculated stiffness and prediction of strength for quantitative CT (QCT) models of human vertebrae [17]. Specimen-specific FE modeling of whole human vertebral bodies is also possible using microcomputed tomography (μCT) at much smaller voxel sizes than QCT, yet larger than the conventional voxel size values used in μCT scanning of cancellous bone specimens. In our experience with μCT scanning of whole human vertebral bodies, scanning voxel sizes of up to 112 μm were required in order to capture the entire specimen (88–112 μm for human vertebrae varying from Thoracic 11 to Lumbar 5, unpublished data). It is desirable to have the capacity to analyze the tissue stresses—as well as density and modulus distributions in whole vertebral bodies—since these analyses may reveal important associations between the ability of tissue to distribute loads and apparent properties, mechanical damage, and anatomical site [18–20]. However, it is not known whether enough cancellous bone structural information is resolved during these scans for studying the aforementioned issues.

Scanning voxel size is intrinsic to the scanning system and scan geometry, and is representative of the level of detail that can be resolved in the image. Reconstruction voxel size determines the level of coarsening from the baseline image, i.e., it represents the sampling effect from the already scanned image. An increase in the reconstruction voxel size is expected to add to the inaccuracies in the image. Reconstruction using voxel sizes greater than scanning voxel size may be required in order to be able to form and solve computer models or to avoid large computational costs. The effects of scanning and reconstruction voxel size have not been considered separately in previous studies where the effect of element size on the FE calculated modulus and stress distributions was investigated [13,14,21,22].

The purpose of the current study was to evaluate the effect of scanning and reconstruction voxel size on the μCT-based FE analyses of human cancellous tissue samples. Combinations of scan/reconstruction voxel size were chosen such that they represent the best possible scans, commonly used intermediate values, and those applicable to *in situ* scans of human vertebrae and other bones of similar size. Our first aim was to determine the change in the magnitude of calculated parameters due to voxel size differences. Our second aim was to determine whether high-resolution model results could be predicted by low-resolution model results. As a third aim, we examined whether FE simulations with fixed- and free-end boundary conditions would have an effect on the calculations.

Methods

Eight cylindrical cancellous bone specimens (10 mm length, 8 mm diameter) were cored in the inferosuperior direction from L2–L4 vertebrae of a 63 year old male and metaphyseal tibia of a 52 year old male. Each of the specimens was μCT scanned at 21 μm, 50 μm, and 110 μm voxel size using a cone–beam system, the details of which were presented previously [23]. Images were reconstructed at 21 μm, 50 μm, and 110 μm resulting in scan/reconstruction combinations of 21/21, 21/50, 21/110, 50/50, 50/110, and 110/110 μm for each specimen. 21 μm is about the best possible scanning voxel size for specimens of this size, 50 μm is a commonly employed intermediate value. The choice of 110 μm was based on our experience with μCT scanning of whole human vertebral bodies and represents a ''best case'' scenario for future *in vivo* scanning of the spine. The 21/21 case was used as the gold standard for determining the level of inaccuracy in the coarser scan/reconstruction combinations.

After reconstruction, bone and nonbone voxels were segmented using a heuristic segmentation algorithm developed specifically for bone tissue with highly nonhomogeneous CT density distributions with a large overlap between bone and bone marrow (Appendix) [24].

Each set of images was used to create linear FE models with a cubic element for each voxel (because of this, element size and reconstruction voxel size can be considered synonymously within the context of our discussions) [25,26]. Inferosuperior compression of the vertebral and tibial cylinders, corresponding to a 0.5% strain was simulated. This simulation is similar to the loading that occurs in life in the vertebrae and tibial metaphysis. Young's modulus of 5 GPa and Poisson's ratio of 0.3 were assumed as trabecular tissue properties for all models (The actual value assumed for Young's modulus does not affect the comparative results) [14,25,27]. Models were run once using free- (simulating frictionless rigid platens) and once using fixed-end (simulating glued specimen ends) boundary conditions resulting in a total of 96 simulations. A special-purpose element by element preconditioned conjugate gradient iterative solver developed in-house was used for the FE analysis [25]. Bone volume fraction (BV/TV) was directly calculated from the μCT images by voxel counting. In addition to the apparent modulus (E), the average, standard deviation, and coefficient of variation of trabecular von Mises stresses (VMExp, VMSD, and COV, respectively) as well as trabecular shear stress amplification (VMExp/σ_z, σ_z: Axial apparent stress generated for the 0.5% axial apparent strain input) were calculated using the FE simulation results. A three-parameter Weibull function fitted to the statistical distribution of the FE-calculated von Mises stress data for each specimen was used for calculating the stress distribution parameters as outlined previously [18,20,28]. The COV of the von Mises stress, which is a measure of trabecular shear stress variability, was calculated as VMSD/VMExp. VMExp/σ_z can be considered as a measure of structural efficiency of the cancellous tissue since it represents the conversion of axial stresses into shear stresses in the trabecular tissue [18,19].

Two-way repeated measures ANOVA was used for analyzing the effect of end boundary conditions and scan/reconstruction combinations with each specimen as the subject and end condition (fixed or free) and scan/reconstruction (21/21,21/50, . . .) as repeated factors (Sigma Stat, SPSS Inc.) When significance was detected, the Bonferroni test was performed to examine the group differences. For further examination of the separate effects of scanning and reconstruction voxel size, two-way RMANOVA was repeated within each end boundary simulation group with scanning voxel size and reconstruction voxel size as repeated factors. To examine the relationship between scanning/reconstruction voxel size and the error in the parameter of concern, Δ (the deviation from the 21/21 case assuming the 21/21 case to be error free) multivariable linear regression was performed. To examine the change in the scatter within a scanning/reconstruction voxel size case, the standard deviation of the error in a parameter of concern was also examined using multivariable linear regression. If either scanning or reconstruction voxel size was significant, only a simple linear regression was performed. It should be noted, however, that measures of statistical significance might not be meaningful for these regressions since the scanning and reconstruction voxel size are not truly random variables. On the other hand, the regression equation itself and the explained variability by the equation might be useful. The relationships between parameters calculated from the 21/21 μm images and those from other combinations of scan/reconstruction voxel size were examined using regression analysis (Microsoft Excel).

Results

BV/TV did not differ considerably between images scanned at 21 and 50 μm and reconstructed at 21, 50, or 110 μm (−0.5% to 7.8% change from the 21/21 μm case, Table 1). For the images scanned and reconstructed at 110 μm, however, there was a large

Table 1 Breakdown of results with scan/recon voxel size and FE end boundary conditions. Average values (standard deviation) are for free- and fixed-end boundary conditions, respectively

Voxel size	BV/TV (%)	E (MPa)	VMExp (MPa)	VMSD (MPa)	COV	VMExp/σ_z
21/21	19.48	247.6	9.429	7.384	0.812	9.409
	(6.11)	(120.0)	(2.450)	(1.033)	(0.144)	(4.770)
		283.4	10.094	8.011	0.827	8.652
		(136.0)	(2.602)	(0.868)	(0.155)	(4.220)
21/50	19.57	245.8	8.935	7.018	0.817	9.516
	(6.05)	(130.5)	(2.562)	(1.235)	(0.148)	(5.337)
		282.0	9.627	7.707	0.838	8.684
		(142.3)	(2.642)	(0.991)	(0.166)	(4.667)
50/50	21.01	293.4	8.833	6.796	0.817	8.405
	(5.95)	(188.0)	(3.282)	(1.706)	(0.160)	(4.883)
		331.7	9.413	7.400	0.844	7.584
		(196.4)	(3.336)	(1.539)	(0.194)	(4.120)
21/110	19.38	231.1	7.688	6.217	0.873	10.385
	(6.72)	(155.5)	(3.263)	(1.975)	(0.192)	(7.174)
		263.5	8.390	6.940	0.899	9.377
		(163.6)	(3.197)	(1.641)	(0.227)	(6.097)
50/110	20.04	269.6	7.550	6.070	0.907	9.804
	(6.82)	(220.6)	(3.911)	(2.286)	(0.248)	(6.872)
		302.8	8.123	6.715	0.939	8.779
		(228.5)	(3.851)	(2.119)	(0.282)	(5.896)
110/110	30.92	312.7	6.595	6.324	1.066	8.558
	(8.85)	(255.0)	(2.816)	(1.839)	(0.341)	(6.956)
		352.5	7.071	6.933	1.094	7.680
		(273.5)	(2.802)	(1.774)	(0.373)	(6.064)

increase in BV/TV compared to the 21/21 μm case (58.7%). A two-way repeated measures ANOVA, with scan and reconstruction voxel size as factors followed by Bonferroni's test, suggested that scanning at 110 μm is the major factor causing the difference ($p<0.001$) whereas reconstruction voxel size did not have a significant effect ($p=0.61$). Consistent with these results, the error in BV/TV increased with increasing scanning voxel size, V_S, ($\Delta\text{BV/TV}(\%)=0.124\,V_S\,(\mu\text{m})-3.41$; $r^2_{\text{adj}}=0.58$, $p<0.001$) but not with reconstruction voxel size, V_R, ($p=0.62$). The scatter of ΔBV/TV within a scan/reconstruction group also increased with scanning voxel size ($\text{SD}_{\Delta\text{BV/TV}}=0.054\,V_S\,(\mu\text{m})+0.208$; $r^2_{\text{adj}}=0.79$, $p<0.02$) but not with reconstruction voxel size ($p=0.11$).

Fixed-end boundary conditions resulted in greater values of E, VMExp, VMSD, and COV but lower values of VMExp/σ_z than the corresponding free-end constraints at the same scan/reconstruction voxel size in all simulations with differences being between 1.8% (COV) and 14.6% (E) (Table 1; $p<0.02$ for all but the COV where $p=0.07$, two-way RMANOVA). Dependence of model output parameters on scanning and reconstruction voxel size was similar between free- and fixed-end simulations. Thus, free-end results only are shown in all figures in the interest of space.

Up to a 26% difference in modulus was observed between the 21/21 μm case and other scan/reconstruction combinations within the same (free or fixed) simulation group (Table 1). However, despite the great percent difference, the variability in the modulus data resulted in statistically nondetectable differences in average values ($p>0.19$ and $p>0.53$ for scan and reconstruction voxel size, respectively). Accordingly, the deviation of E from the 21/21 μm case (ΔE) was not predicted by scanning voxel size ($p=0.13$) or reconstruction voxel size ($p=0.66$). When normalized by BV/TV, the results were still nonsignificant ($p>0.16$ for all). The scatter in ΔE, on the other hand, was related to both scanning voxel size and reconstruction voxel size ($\text{SD}_{\Delta E}\,(\text{MPa})=1.616\,V_S\,(\mu\text{m})+0.934\,V_R\,(\mu\text{m})-45.383$; $r^2_{\text{adj}}=0.94$, $p_{\text{model}}<0.01$; $p<0.02$, and $p<0.04$ for scanning and reconstruction voxel size, respectively). Consistent with this result, ΔE increased with increasing scanning voxel size ($\Delta E(\%)=0.825\,V_S\,(\mu\text{m})-18.461$; $r^2_{\text{adj}}=0.791$, $p<0.02$) when averaged over eight observations for a given scan/reconstruction combination. Together, these results indicate that the nonsignificance of the average difference in modulus from the 21/21 μm case was caused by the increasing variability of values with increasing scanning and reconstruction voxel size.

The differences in the average (VMExp, up to 30%) and standard deviation (VMSD, up to 17.8%) of trabecular shear stresses were largely attributable to reconstruction voxel size ($p<0.006$) rather than scanning voxel size ($p>0.21$) in both free- and fixed-end simulations. Consistent with the ANOVA results, the deviations of VMExp and VMSD from the 21/21 μm case were predictable from reconstruction voxel size but the explained variability was low ($\Delta\text{VMExp}\,(\text{MPa})=-0.025\,V_R\,(\mu\text{m})+0.635$; $r^2_{\text{adj}}=0.18$, $p<0.002$, and $\Delta\text{VMSD}\,(\text{MPa})=-0.013\,V_R\,(\mu\text{m})+0.203$; $r^2_{\text{adj}}=0.20$, $p<0.001$). The deviations of VMExp and VMSD from the 21/21 μm case were not predictable from scanning voxel size ($p=0.23$ and $p=0.87$ for VMExp and VMSD, respectively). The scatter of ΔVMExp within a scan/reconstruction group increased with reconstruction voxel size ($\text{SD}_{\Delta\text{VMExp}}\,(\text{MPa})=0.026\,V_R\,(\mu\text{m})-0.41$; $r^2_{\text{adj}}=0.73$, $p<0.02$) but not with scanning voxel size ($p=0.21$). Similarly, the scatter in ΔVMSD increased with reconstruction voxel size ($\text{SD}_{\Delta\text{VMSD}}\,(\text{MPa})=0.013\,V_R\,(\mu\text{m})-0.187$; $r^2_{\text{adj}}=0.81$, $p<0.01$) but not with scanning voxel size ($p=0.62$). When averaged over eight observations for a given scan/reconstruction combination, ΔVMExp was related to both scanning and reconstruction voxel sizes ($\Delta\text{VMExp}\,(\text{MPa})=-0.012\,V_S\,(\mu\text{m})-0.02\,V_R\,(\mu\text{m})+0.791$; $r^2_{\text{adj}}=0.97$, $p<0.003$), further reinforcing the effect of data scattering by voxel size on predicting group averages. When normalized by BV/TV, both scanning and reconstructing at 110 μm resulted in significant differences in the average and standard deviation of the von Mises stress with respect to the 21 μm and 50 μm scan/reconstruction combinations ($p<0.03$ for all).

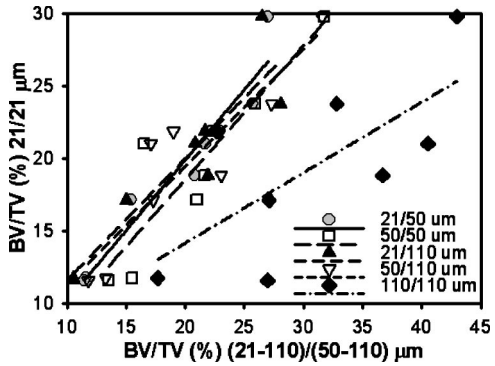

Fig. 1 Prediction of BV/TV calculated from 21/21 mm images by BV/TV calculated from other combinations of scan/reconstruction voxel size. All relationships are significant (Table 2).

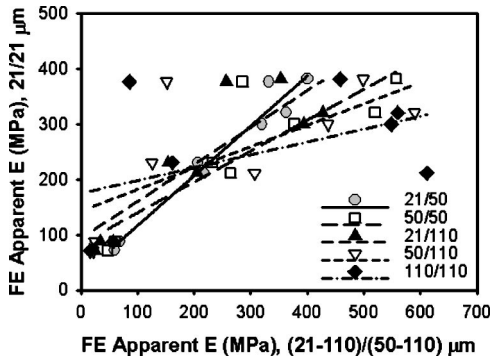

Fig. 2 Prediction of FE apparent modulus (*E*) calculated from 21/21 μm images by *E* calculated from other combinations of scan/reconstruction voxel size. All relationships except for 110/110 μm are significant (Table 2).

Up to 32.3% differences in COVs between 21/21 μm and other scan/reconstruction combinations (110/110 μm being largest) originated from significant differences between 110/110 and three other cases of 21/21, 21/50, and 50/50 μm ($p<0.02$; two-way RMANOVA). The difference between the 110/110 and the other groups were related, but only marginally, to both scan and reconstruction voxel size ($p=0.084$ and $p=0.066$, respectively, within the fixed-end simulations; $p=0.053$ and $p=0.062$, respectively, within the free-end simulations). A regression analysis indicated that the deviation of COV from the 21/21 case was predictable, though weakly, from scanning voxel size ($\Delta\text{COV} = 0.003\,V_S\,(\mu\text{m}) - 0.045$; $r^2_{\text{adj}}=0.17$, $p<0.003$) but not from reconstruction voxel size ($p=0.25$). The scatter in ΔCOV was related to both scanning voxel size and reconstruction voxel size ($\text{SD}_{\Delta\text{COV}} = 0.003\,V_S\,(\mu\text{m}) + 0.001\,V_R\,(\mu\text{m}) - 0.098$; $r^2_{\text{adj}}=0.99$, $p_{\text{model}}<0.001$; $p<0.001$ and $p<0.004$ for scanning and reconstruction voxel size, respectively). When normalized with BV/TV, COV was not related to scanning or reconstruction voxel size ($p>0.12$ and $p>0.08$ for scanning and reconstruction voxel size, respectively, for both free and fixed end).

VMExp/σ_z was not different between scan/reconstruction combinations ($p=0.117$). When normalized by BV/TV, scanning at 110 μm was a significant factor affecting VMExp/σ_z ($p<0.03$; Bonferroni test; $p<0.03$ and $p>0.10$ for scan and reconstruction voxel size, respectively, for both free and fixed end; RMANOVA). Multivariable linear regression showed that the deviation of VMExp/σ_z from the 21/21 case was significantly related to scanning voxel size ($p=0.02$) but not to reconstruction voxel size ($p=0.14$). When averaged over eight observations reducing the noise, ΔVMExp/σ_z was predictable from both scanning and reconstruction voxel sizes ($\Delta\text{VMExp}/\sigma_z = -0.022\,V_S\,(\mu\text{m}) + 0.015\,V_R\,(\mu\text{m}) - 0.16$; $r^2_{\text{adj}}=0.80$, $p<0.05$). The scatter of ΔVMExp/σ_z increased with both scanning voxel size and reconstruction voxel size ($\text{SD}_{\Delta\text{VMExp}/\sigma_z} = 0.011\,V_S\,(\mu\text{m}) + 0.028\,V_R\,(\mu\text{m}) - 0.939$; $r^2_{\text{adj}}=0.98$, $p_{\text{model}}<0.002$; $p<0.05$ and $p<0.002$ for scanning and reconstruction voxel size, respectively).

All 21/21 μm results (taken as the gold standard) could be predicted from the 21/50 ($r^2_{\text{adj}}=0.91-0.99; p<0.001$), 21/110 ($r^2_{\text{adj}}=0.58-0.99; p<0.02$) and 50/50 results ($r^2_{\text{adj}}=0.61-0.97; p<0.02$) (Table 2, Figs. 1–6). While BV/TV, VMSD, and VMExp/σ_z from the 21/21 could be predicted by those from the 50/110 ($r^2_{\text{adj}}=0.63-0.93; p<0.02$) and 110/110 ($r^2_{\text{adj}}=0.41-0.77; p<0.05$) simulations as well, prediction of *E*, VMExp, and COV became marginally significant ($0.04<p<0.13$) at 50/110 and nonsignificant at 110/110 ($0.21<p<0.70$).

Discussion

The effect of scanning and reconstruction voxel size on the calculation of BV/TV, apparent modulus and stress distribution parameters were examined for μCT-based large-scale FE models of human cancellous bone with free- and fixed-end boundary conditions. Bone volume fraction is not a FE parameter but was in-

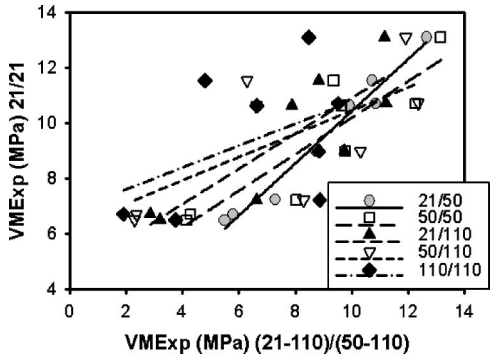

Fig. 3 Prediction of the average trabecular von Mises stress (VMExp) calculated from 21/21 μm images by VMExp calculated from other combinations of scan/reconstruction voxel size. The 110/110 μm case is nonsignificant and the 50/110 μm case is only marginally significant (Table 2).

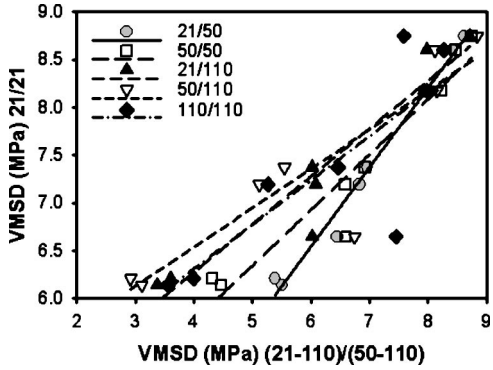

Fig. 4 Prediction of the standard deviation of trabecular von Mises stress (VMSD) calculated from 21/21 μm images by VMSD calculated from other combinations of scan/reconstruction voxel size. All relationships are significant (Table 2).

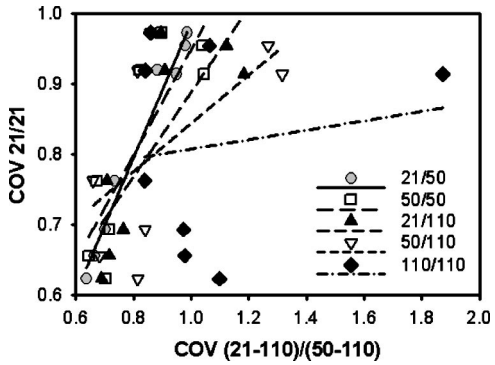

Fig. 5 Prediction of the coefficient of variation of trabecular von Mises stress (COV) calculated from 21/21 μm images by COV calculated from other combinations of scan/reconstruction voxel size. All relationships except for the 50/110 μm and 110/110 μm cases are significant (Table 2).

cluded in the analysis to gain insight into whether the observed changes in FE parameters are attributable solely to changes in BV/TV.

With large bone and joint segments, particularly whole vertebral bodies in mind, the 110 μm scanning and reconstruction voxel size was chosen to establish an upper bound ''best'' voxel size based on our experience with μCT scanning of whole human vertebral bodies. The images scanned and reconstructed at 21 μm were considered as the gold standard for the study. 21 μm is about as small a voxel size as possible for our specimens (10 mm long cylinders with 8 mm diameter). It is possible to acquire images at smaller voxel sizes with our microtomography system if smaller specimen sizes are used. However, better than a 20 μm element size may not be necessary for the purpose of our study as it has been shown that 20 μm is sufficient for accurately calculating human cancellous bone modulus including specimens from low-density regions such as vertebral bone [15] and smaller voxel sizes may not significantly improve this accuracy [29]. The 10×8 mm cylinder is also our standard mechanical test geometry for cancellous bone [26,30,31]. Because it is desirable to test these specimens mechanically in future studies and the scanning resolution is sufficient to resolve enough microstructural details for calculating bone properties, the choice of specimen size is reasonable.

The current study did not examine the separate effects of segmentation on the measured parameters. Segmentation of bone voxels from nonbone voxels is a necessary step in voxel-based FE models that utilize μCT images. Usually, global thresholding algorithms (thresholding using a single value above which is deemed bone and below which is deemed nonbone) are used in the analysis of cancellous bone; an approach taken by our group and by others in the past [13,14,18,19,25,26,32]. It is known that the resultant bone structure (hence, FE solutions) can be sensitive to the selection of the threshold value [33,34]. It has been suggested that the threshold value should be forced to compensate for the loss of trabeculae by maintaining the ''original'' BV/TV value that must be determined from an available high-resolution image of the same specimen [35] or adjusted using a BV/TV value from an independent reference measurement, such as one based on Archimedes' principle [36]. Because we were interested in determining the overall effect of scanning and reconstruction voxel size from an image as it is in the assumed absence of a priori knowledge of the actual BV/TV, we did not force our images to match with a known reference value.

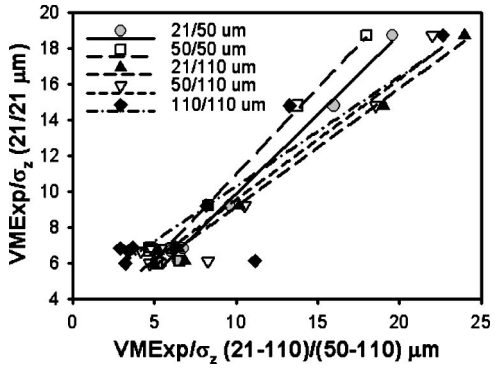

Fig. 6 Prediction of the shear stress amplification (VMExp/σ_z) calculated from 21/21 μm images by VMExp/σ_z calculated from other combinations of scan/reconstruction voxel size. All relationships are significant (Table 2).

Direct use of gray values in FE models in order to circumvent the problems associated with thresholding has been suggested recently [37]. Although this is a potentially powerful approach, the accuracy of the results from this method is highly sensitive to the choice of parameters that are used for converting gray levels to tissue properties. These parameters are not available for general application and need to be estimated (or calibrated through separate studies) for various anatomical sites. The gray-value method does not need a distinction between bone and nonbone voxels for running FE models, however, an analysis of trabecular microarchitecture may still require some form of segmentation. Nonetheless, future work should consider this alternative approach.

In addition to the variation in BV/TV and apparent modulus, the variation in the von Mises shear stress statistics were examined. The choice of von Mises stress as a study parameter—among many other potentially important stress/strain measures—was based on our previous work where it was established that the von Mises stress is associated with cancellous bone microdamage, and is potentially important in explaining anatomical and donor-specific variations in vertebral bone strength [18–20,30,38]. It should be noted, however, that although the ability of models to capture trabecular stress statistics is indicative of how well the spatial distribution of stresses in the cancellous tissue is represented in models, this study did not address how resolution affects the spatial distribution of stresses or other parameters within the trabecular microstructure. This may be important for applications where the relationship of local mechanical parameters with cellular responses is of interest.

A number of studies investigated the effect of voxel size on bone microstructural parameters calculated from CT images and on the computed values of bone properties in FE simulations [13,14,21,22,39]. However, the larger element sizes used in FE models were obtained either by coarsening a higher-resolution μCT image of the specimen rather than rescanning the specimen at the desired coarse resolution, or by rescanning and reconstructing at a low resolution, or by another instrument, such as pQCT, in those studies. The current study used both coarsened and rescanned images of the same specimen providing the opportunity to distinguish between the effects of scanning and reconstruction voxel size for μCT applications. This study also provided significant insight into the variability of these effects by utilizing eight different specimens.

The calculation of cancellous bone modulus, mean trabecular stress, and other parameters is subject to large errors at 110/110 μm voxel size (Table 1, Figs. 1–6). However, our results indicate that enough microstructural details for studying BV/TV, trabecular shear stress scatter, and trabecular shear stress amplification (VMExp/σ_z) can be resolved using 21/110 μm, 50/110 μm, and 110/110 μm voxels for both free- and fixed-end constraints (Tables 1 and 2, Figs. 4 and 6). In a similar study, it has been found that BV/TV and three-dimensional (3D) microstructural parameters of cancellous bone calculated from 165 μm pQCT scans could predict those from 28 μm μCT scans of the same specimen

Table 2 Regressions between the 21/21 case and other scan/reconstruction voxel size cases for each parameter. Fixed-end simulations had similar results in terms of significance and explanatory capability. Therefore, reported results are for the free-end simulations only, except for BV/TV which is independent of the type of FE model. If the slope of the regression was significant but the intercept was not, another linear model was applied to the data forcing the fit through the origin. For the latter, *p* values associated with the regression are reported.

Y 21/21	21/50	50/50	21/110	50/110	110/110
BV/TV (%)	$0.973\,X+0.445$ $r^2_{adj}=0.91$ $p_{slope}<0.001$ $p_{int}>0.85$ $0.994\,X$ $r^2_{adj}=0.78$ $p_{reg}<0.001$	$0.925\,X+0.0476$ $r^2_{adj}=0.78$ $p_{slope}=0.002$ $p_{int}>0.99$ $0.927\,X$ $r^2_{adj}=0.67$ $p_{reg}<0.001$	$0.840\,X+3.193$ $r^2_{adj}=0.83$ $p_{slope}<0.001$ $p_{int}>0.3$ $0.989\,X$ $r^2_{adj}=0.68$ $p_{reg}<0.001$	$0.814\,X+3.164$ $r^2_{adj}=0.80$ $p_{slope}=0.002$ $p_{int}>0.36$ $0.958\,X$ $r^2_{adj}=0.65$ $p_{reg}<0.002$	$0.487\,X+4.429$ $r^2_{adj}=0.41$ $p_{slope}=0.0501$ $p_{int}>0.51$ $0.651\,X$ $r^2_{adj}=0.31$ $p_{reg}=0.052$
E (MPa)	$0.900\,X+26.3$ $r^2_{adj}=0.95$ $p_{slope}<0.001$ $p_{int}>0.26$ $0.986\,X$ $r^2_{adj}=0.80$ $p_{reg}<0.001$	$0.558\,X+84.0$ $r^2_{adj}=0.72$ $p_{slope}<0.005$ $p_{int}>0.10$ $0.768\,X$ $r^2_{adj}=0.47$ $p_{reg}<0.02$	$0.668\,X+93.3$ $r^2_{adj}=0.71$ $p_{slope}<0.006$ $p_{int}>0.07$ $0.957\,X$ $r^2_{adj}=0.41$ $p_{reg}<0.03$	$0.387\,X+143.4$ $r^2_{adj}=0.42$ $p_{slope}<0.05$ $p_{int}<0.04$	NS $p_{slope}>0.21$
VMExp (MPa)	$0.943\,X+1.005$ $r^2_{adj}=0.97$ $p_{slope}<0.001$ $p_{int}>0.14$ $1.048\,X$ $r^2_{adj}=0.82$ $p_{reg}<0.001$	$0.660\,X+3.597$ $r^2_{adj}=0.78$ $p_{slope}<0.004$ $p_{int}<0.04$	$0.639\,X+4.519$ $r^2_{adj}=0.68$ $p_{slope}<0.008$ $p_{int}<0.02$	$0.420\,X+6.255$ $r^2_{adj}=0.36$ $p_{slope}=0.069$	NS $p_{slope}>0.25$
VMSD (MPa)	$0.830\,X+1.559$ $r^2_{adj}=0.98$ $p_{slope}<0.001$ $p_{int}<0.002$	$0.581\,X+3.437$ $r^2_{adj}=0.91$ $p_{slope}<0.001$ $p_{int}<0.001$	$0.501\,X+4.268$ $r^2_{adj}=0.90$ $p_{slope}<0.001$ $p_{int}<0.001$	$0.410\,X+4.895$ $r^2_{adj}=0.79$ $p_{slope}<0.002$ $p_{int}<0.001$	$0.463\,X+4.457$ $r^2_{adj}=0.68$ $p_{slope}<0.02$ $p_{int}<0.002$
COV	$0.959\,X+0.028$ $r^2_{adj}=0.97$ $p_{slope}<0.001$ $p_{int}>0.62$ $0.993\,X$ $r^2_{adj}=0.83$ $p_{reg}<0.001$	$0.750\,X+0.199$ $r^2_{adj}=0.65$ $p_{slope}<0.01$ $p_{int}>0.27$ $0.986\,X$ $r^2_{adj}=0.47$ $p_{reg}<0.02$	$0.601\,X+0.287$ $r^2_{adj}=0.58$ $p_{slope}<0.02$ $p_{int}>0.12$ $0.917\,X$ $r^2_{adj}=0.32$ $p_{reg}=0.0507$	$0.343\,X+0.502$ $r^2_{adj}=0.24$ $p_{slope}=0.122$	NS $p_{slope}>0.7$
VMExp/σ_z	$0.891\,X+0.929$ $r^2_{adj}=0.99$ $p_{slope}<0.001$ $p_{int}<0.03$	$0.964\,X+1.307$ $r^2_{adj}=0.97$ $p_{slope}<0.001$ $p_{int}>0.07$ $1.084\,X$ $r^2_{adj}=0.81$ $p_{reg}<0.001$	$0.662\,X+2.539$ $r^2_{adj}=0.99$ $p_{slope}<0.001$ $p_{int}<0.001$	$0.674\,X+2.798$ $r^2_{adj}=0.93$ $p_{slope}<0.001$ $p_{int}<0.02$	$0.614\,X+4.156$ $r^2_{adj}=0.77$ $p_{slope}<0.003$ $p_{int}<0.03$

[21]. Our finding that BV/TV calculated from 110/110 μm images predicts that from 21/21 μm calculations is consistent with this report. However, apparent modulus calculated from 110/110 μm images did not predict that from 21/21 μm images in the current study. This may suggest that although the average microstructural information is preserved in coarse models, subtle differences in the distribution of microstructures may cause substantial changes in the apparent modulus [40]. The success of low-resolution models (165 μm voxel size) in predicting bone fracture or higher-resolution model outputs might be, in part, attributable to the presence of considerable external geometry, such as that in distal radius and proximal femur [39,41]. A 110/110 μm μCT model of a whole vertebral body might also be successful in predicting vertebral fracture.

Our results indicate that significant information on the scatter and amplification of trabecular shear stress is extractable using a large voxel size which will permit studying shear stress amplification in whole bones [19]. This could be significant as shear stress amplification (VMExp/σ_z) is predictive of *in vivo* tissue damage [19] and is a parameter that increases with age in human vertebral cancellous bone (unpublished; reanalysis of published data [18]). We have reported in a previous study that shear stress amplification in cancellous bone tissue decreased from thoracic-4 through T12-lumbar 1 levels and increased afterward, the trend being characterized by a quadratic relationship between stress amplification and spine levels when vertebrae were assigned numbers representing their anatomical location in the spine [18]. Thus, the ability to study this parameter in whole bones is also significant in that VMExp/σ_z may be a mechanistic pathway to explain the differences in the propensity to fracture between bones from different spine levels [18].

The current results demonstrate that it is the resolution of raw data that primarily determines the accuracy of models as BV/TV was mostly affected by the scanning resolution. Final reconstructed voxel size contributed to the inaccuracy moderately, at least up to the 100 micrometer reconstruction of cancellous bone data at which the differences were drastic. The finding that coarsening by the reconstruction of a high-resolution scan has less influence on the outcome than scanning at a low resolution might be, in part, due to presence of higher signal-to-noise ratio in the latter. Changes in the BV/TV did not fully account for the changes in FE-calculated parameters, indicating that the inaccuracy of low-resolution models is not simply due to increased density caused by thickening of trabeculae.

While necessary to demonstrate, it is not completely surprising that the scanning resolution has a more prominent effect on results as it is the raw data resolution that determines the ability of the CT software to sustain high-resolution reconstruction. As a result, large voxel size reconstructions built from high-resolution data partake in much the accuracy of the underlying data. As noted above, this fact will permit the accurate study of large physical size FE models without the ordinarily expected loss of information usually believed to be associated with the larger voxel size used for the models. A final note is that the microtomography system used in this study was that described in detail by Reimann et al. [23]. To what extent our results are applicable to other models of μCT may need further elucidation.

Acknowledgment

Support from the National Institutes of Health is gratefully acknowledged: AR049343 (YNY) and AR40776 (DPF).

Appendix

Thresholding of μCT images, i.e., segregating bone from marrow and background noise is usually straightforward with tissue that has a relatively more uniform structure using a global threshold [32]. However, the X-ray intensity distribution in vertebral body images from μCT scans has a higher variability relative to that in more homogeneous specimens such as cancellous bone cores. This makes it difficult to segregate bone from marrow and background noise using customary methods that are based on determining a single (global) threshold value.

Our heuristic algorithm for thresholding applies five successive processes to the μCT data: Normalization, edge detection, continuity crawling, final thresholding, and connectivity testing.

Normalization calculates a new value for each voxel that tends to bring local maxima to the same level. A global minimum value is calculated as the second percentile of a 0.2% sample in the bone core. Working in $5\times5\times5$-voxel subcubes, a local maximum value is found for the surrounding $25\times25\times25$-voxel neighborhood. For each voxel in the subcube, the value is linearly mapped between the local maximum and the global minimum. To facilitate visual comparison, the new value is scaled to match the old intensity range.

Edge detection searches for high contrast. For each voxel, the normalized data are searched over a range of five voxels parallel to each axis in the positive and negative direction (six searches) for a value that is more than 50% different from the base voxel. If such a condition is found, the higher level is deemed ''bone'' and the lower level ''nonbone.''

Continuity crawling extends the bone and nonbone found by edge detection. Using the original μCT data, each voxel is compared to its six face neighbors. If a face neighbor is bone and has an intensity value less than or equal to that of the base voxel, the base voxel is deemed bone. If a face neighbor is nonbone and has an intensity value greater than or equal to that of the base voxel, the base voxel is deemed nonbone. The recursion continues until no more changes are found.

Edge detection and continuity crawling are iterated with contrast levels of 40%, 30%, and 20% to identify successively more bone and nonbone.

Final thresholding is applied to voxels left undetermined by the above steps. For each undetermined voxel, mean bone and nonbone values are calculated for the entire volume using reciprocal-distance-squared weighted averaging. If the undetermined voxel is above the midpoint of the two means, it is deemed bone. If not, it is deemed nonbone.

Connectivity testing removes ''loose pieces.'' A $10\times10\times10$-voxel cube of solid bone is found as a starting point. Bone voxels are grown recursively in each direction using a face-connectivity rule.

We have shown that this method produces at least visually satisfactory segmented images of human vertebral bodies where a global thresholding algorithm resulted in either the loss of thinner and/or more interior features (cancellous bone) or the thickening of larger and/or more exterior features (shell) [24]. In addition, μCT images that could not be thresholded previously due to a very high overlap between the x-ray intensity of noise and bone were re-examined using the new algorithm (human T12 vertebral cancellous bone cores; three males, seven females, 61 ± 17 years old). BV/TV calculated from these images was consistent with previously reported values from human T12 vertebrae (0.112 ± 0.037) [25], whereas attempts to threshold them using a single value resulted in thickened and compacted images and BV/TV values about three times larger than expected.

We have analyzed an additional group of human cancellous bone specimens (eight vertebral and ten tibial) that had ''normal'' μCT images. We found that BV/TV and E_{FEM} calculated from images segmented using a single threshold were highly correlated with those calculated from images segmented using the heuristic method for normal images of human cancellous bone tissue ($\mathrm{BV/TV}_{\mathrm{heuristic}}=0.718\,\mathrm{BV/TV}_{\mathrm{single}}$; $r^2_{\mathrm{adj}}=0.66$, $p<0.001$ and $E_{\mathrm{FEMheuristic}}=0.588\,E_{\mathrm{FEMsingle}}$; $r^2_{\mathrm{adj}}=0.71$, $p<0.001$).

Although there are systematic differences between calculations from images processed with a single threshold and those from images processed using the heuristic segmentation, the high correlation between the two suggest that the use of either one is acceptable in a comparative study. The real value of the latter method is more apparent when applied to different problems, however, this is beyond the scope of the current study.

References

[1] Tosteson, A., 2000, In *NIH Concensus Development Conference on Osteoporosis Prevention, Diagnosis, and Therapy*, NIH, Bethesda, MD, pp. 65–66.

[2] Gallagher, J. C., Melton, L. J., Riggs, B. L., and Bergstrath, E., 1980, ''Epidemiology of Fractures of the Proximal Femur in Rochester, Minnesota,'' Clin. Orthop., **150**, pp. 163–171.

[3] Cummings, S. R., Kelsey, J. L., Nevitt, M. C., and O'Dowd, K. J., 1985, ''Epidemiology of Osteoporosis and Osteoporotic Fractures,'' Epidemiol. Rev., **7**, pp. 178–208.

[4] Melton, III, L. J., Lane, A. W., Cooper, C., Eastell, R., O'Fallon, W. M., and Riggs, B. L., 1993, ''Prevalence and Incidence of Vertebral Deformities,'' Osteoporosis Int., **3**, pp. 113–119.

[5] Ross, P. D., 1997, ''Clinical Consequences of Vertebral Fractures,'' Am. J. Med., **103**, pp. 30S–42S; discussion 42S–43S.

[6] Nevitt, M. C., Ross, P. D., Palermo, L., Musliner, T., Genant, H. K., and Thompson, D., 1999, ''Association of Prevalent Vertebral Fractures, Bone Density, and Alendronate Treatment With Incident Vertebral Fractures: Effect of Number and Spinal Location of Fractures,'' Bone (N.Y.), **25**, pp. 613–619.

[7] Kanis, J. A., Melton, III, L. J., Christiansen, C., Johnston, C. C., and Khaltaev, N., 1994, ''The Diagnosis of Osteoporosis,'' J. Bone Miner. Res., **9**, pp. 1137–1141.

[8] Silva, M. J., Keaveny, T. M., and Hayes, W. C., 1997, ''Load Sharing Between the Shell and Centrum in the Lumbar Vertebral Body,'' Spine, **22**, pp. 140–150.

[9] Bryce, R., Aspden, R. M., and Wytch, R., 1995, ''Stiffening Effects of Cortical Bone on Vertebral Cancellous Bone *in situ*,'' Spine, **20**, pp. 999–1003.

[10] Andresen, R., Werner, H. J., and Schober, H. C., 1998, ''Contribution of the Cortical Shell of Vertebrae to Mechanical Behavior of the Lumbar Vertebrae With Implications for Predicting Fracture Risk,'' Br. J. Radiol., **71**, pp. 759–765.

[11] Liebschner, M. A., Kopperdahl, D. L., Rosenberg, W. S., and Keaveny, T. M., 2003, ''Finite Element Modeling of the Human Thoracolumbar Spine,'' Spine, **28**, pp. 559–565.

[12] Mizrahi, J., Silva, M. J., Keaveny, T. M., Edwards, W. T., and Hayes, W. C., 1993, ''Finite-Element Stress Analysis of the Normal and Osteoporotic Lumbar Vertebral Body,'' Spine, **18**, pp. 2088–2096.

[13] Niebur, G. L., Yuen, J. C., Hsia, A. C., and Keaveny, T. M., 1999, ''Convergence Behavior of High-Resolution Finite Element Models of Trabecular Bone,'' J. Biomech. Eng., **121**, pp. 629–635.

[14] van Rietbergen, B., Weinans, H., Huiskes, R., and Odgaard, A., 1995, ''A New Method to Determine Trabecular Bone Elastic Properties and Loading Using Micromechanical Finite-Element Models,'' J. Biomech., **28**, pp. 69–81.

[15] Ladd, A. J., and Kinney, J. H., 1998, ''Numerical Errors and Uncertainties in Finite-Element Modeling of Trabecular Bone,'' J. Biomech., **31**, pp. 941–945.

[16] Keyak, J. H., and Skinner, H. B., 1992, ''Three-Dimensional Finite Element Modeling of Bone: Effects of Element Size,'' J. Biomech. Eng., **14**, pp. 483–489.

[17] Crawford, R. P., Rosenberg, W. S., and Keaveny, T. M., 2003, ''Quantitative

Computed Tomography-Based Finite Element Models of the Human Lumbar Vertebral Body: Effect of Element Size on Stiffness, Damage, and Fracture Strength Predictions,'' J. Biomech. Eng., **125**, pp. 434–438.
[18] Yeni, Y. N., Hou, F. J., Vashishth, D., and Fyhrie, D. P., 2001, ''Trabecular Shear Stress in Human Vertebral Cancellous Bone: Intra- and Interindividual Variations,'' J. Biomech., **34**, pp. 1341–1346.
[19] Yeni, Y. N., Hou, F. J., Ciarelli, T., Vashishth, D., and Fyhrie, D. P., 2003, ''Trabecular Shear Stresses Predict *In Vivo* Linear Microcrack Density but not Diffuse Damage in Human Vertebral Cancellous Bone,'' Ann. Biomed. Eng., **31**, pp. 726–732.
[20] Fyhrie, D. P., Hoshaw, S. J., Hamid, M. S., and Hou, F. J., 2000, ''Shear Stress Distribution in the Trabeculae of Human Vertebral Bone,'' Ann. Biomed. Eng., **28**, pp. 1194–1199.
[21] Laib, A., and Ruegsegger, P., 1999, ''Calibration of Trabecular Bone Structure Measurements of *In Vivo* Three-Dimensional Peripheral Quantitative Computed Tomography With 28-Micrometer-Resolution Microcomputed Tomography,'' Bone (N.Y.), **24**, pp. 35–39.
[22] Jacobs, C. R., Davis, B. R., Rieger, C. J., Francis, J. J., Saad, M., and Fyhrie, D. P., 1999, ''The Impact of Boundary Conditions and Mesh Size on the Accuracy of Cancellous Bone Tissue Modulus Determination Using Large-Scale Finite-Element Modeling,'' J. Biomech., **32**, pp. 1159–1164.
[23] Reimann, D. A., Hames, S. M., Flynn, M. J., and Fyhrie, D. P., 1997, ''A Cone Beam Computed Tomography System for True 3D Imaging of Specimens,'' Appl. Radiat. Isot., **48**, pp. 1433–1436.
[24] Zauel, R., Yeni, Y. N., Christopherson, G. T., Cody, D. D., and Fyhrie, D. P., 2004, in *50th Annual Meeting, Orthopaedic Research Society* 1018, San Francisco, Ca.
[25] Hou, F. J., Lang, S. M., Hoshaw, S. J., Reimann, D. A., and Fyhrie, D. P., 1998, ''Human Vertebral Body Apparent and Hard Tissue Stiffness,'' J. Biomech., **31**, pp. 1009–1015.
[26] Yeni, Y. N., and Fyhrie, D. P., 2001, ''Finite Element Calculated Uniaxial Apparent Stiffness is a Consistent Predictor of Uniaxial Apparent Strength in Human Vertebral Cancellous Bone Tested With Different Boundary Conditions,'' J. Biomech., **34**, pp. 1649–1654.
[27] Ladd, A. J., Kinney, J. H., Haupt, D. L., and Goldstein, S. A., 1998, ''Finite-Element Modeling of Trabecular Bone: Comparison With Mechanical Testing and Determination of Tissue Modulus,'' J. Orthop. Res., **16**, pp. 622–628.
[28] Bury, K., 1999, *Statistical Distributions in Engineering*, Cambridge University Press, Cambridge, UK.
[29] Peyrin, F., Salome, M., Cloetens, P., Laval-Jeantet, A. M., Ritman, E., and Ruegsegger, P., 1998, ''Micro-CT Examinations of Trabecular Bone Samples at Different Resolutions: 14, 7, and 2 Micron Level,'' Technol. Health Care, **6**, pp. 391–401.
[30] Fyhrie, D. P., and Schaffler, M. B., 1994, ''Failure Mechanisms in Human Vertebral Cancellous Bone,'' Bone (N.Y.), **15**, pp. 105–109.
[31] Fyhrie, D. P., and Vashishth, D., 2000, ''Bone Stiffness Predicts Strength Similarly for Human Vertebral Cancellous Bone in Compression and for Cortical Bone in Tension,'' Bone (N.Y.), **26**, pp. 169–173.
[32] Kuhn, J. L., Goldstein, S. A., Feldkamp, L. A., Goulet, R. W., and Jesion, G., 1990, ''Evaluation of a Microcomputed Tomography System to Study Trabecular Bone Structure,'' J. Orthop. Res., **8**, pp. 833–842.
[33] Ito, M., Nakamura, T., Matsumoto, T., Tsurusaki, K., and Hayashi, K., 1998, ''Analysis of Trabecular Microarchitecture of Human Iliac Bone Using Microcomputed Tomography in Patients With Hip Arthrosis With or Without Vertebral Fracture,'' Bone (N.Y.), **23**, pp. 163–169.
[34] Hara, T., Tanck, E., Homminga, J., and Huiskes, R., 2002, ''The Influence of Microcomputed Tomography Threshold Variations on the Assessment of Structural and Mechanical Trabecular Bone Properties,'' Bone (N.Y.), **31**, 107–109.
[35] Ulrich, D., van Rietbergen, B., Weinans, H., and Ruegsegger, P., 1998, ''Finite Element Analysis of Trabecular Bone Structure: A Comparison of Image-Based Meshing Techniques,'' J. Biomech., **31**, pp. 1187–1192.
[36] Ding, M., Odgaard, A., and Hvid, I., 1999, ''Accuracy of Cancellous Bone Volume Fraction Measured by Micro-CT Scanning,'' J. Biomech., **32**, 323–326.
[37] Homminga, J., Huiskes, R., Van Rietbergen, B., Ruegsegger, P., and Weinans, H., 2001, ''Introduction and Evaluation of a Gray-Value Voxel Conversion Technique,'' J. Biomech., **34**, pp. 513–517.
[38] Yeni, Y. N., Vashishth, D., and Fyhrie, D. P., 2001, in *Summer Bioengineering Conference, the American Society of Mechanical Engineers*, ASME, N.Y., pp. 19–20.
[39] Pistoia, W., van Rietbergen, B., Lochmuller, E. M., Lill, C. A., Eckstein, F., and Ruegsegger, P., 2002, ''Estimation of Distal Radius Failure Load With Microfinite Element Analysis Models Based on Three-Dimensional Peripheral Quantitative Computed Tomography Images,'' Bone (N.Y.), **30**, 842–848.
[40] Yeh, O. C., and Keaveny, T. M., 1999, ''Biomechanical Effects of Intraspecimen Variations in Trabecular Architecture: A Three-Dimensional Finite Element Study,'' Bone (N.Y.), **25**, 223–228.
[41] Pistoia, W., van Rietbergen, B., Laib, A., and Ruegsegger, P., 2001, ''High-Resolution Three-Dimensional-*p*QCT Images can be an Adequate Basis for *In Vivo* MicroFE Analysis of Bone,'' J. Biomech. Eng., **123**, pp. 176–183.